bioRxiv preprint doi: https://doi.org/10.1101/385799; this version posted August 6, 2018. The copyright holder for this preprint (which was not certified by peer review) is the author/funder. All rights reserved. No reuse allowed without permission.

Combining 3D single molecule localization strategies for reproducible bioimaging

Clément Cabriel[1,*], Nicolas Bourg[1], Pierre Jouchet[1], Guillaume Dupuis[2], Christophe Leterrier[3], Aurélie Baron[4], Marie-Ange Badet-Denisot[4], Boris Vauzeilles[4,5], Emmanuel Fort[6], and Sandrine Lévêque-Fort[1,**]

[1]Institut des Sciences Moléculaires d'Orsay (ISMO), CNRS UMR 8214, Université Paris-Sud, bâtiment 520, rue André Rivière, 91405 Orsay Cedex, France
[2]Centre de Photonique BioMédicale (CPBM), CNRS FR 2764, Fédération LUMAT, Université Paris-Sud, bâtiment 520, rue André Rivière, 91405 Orsay Cedex, France
[3]Aix-Marseille Université, CNRS, INP UMR7051, Marseille, France
[4]Centre de Recherche de Gif, Institut de Chimie des Substances Naturelles du CNRS, Gif-sur-Yvette, France
[5]Laboratoire de Synthèse de Biomolécules, Institut de Chimie Moléculaire et des Matériaux d'Orsay, Université Paris-Sud, CNRS UMR 8182, Orsay, France
[6]Institut Langevin, ESPCI ParisTech, CNRS, PSL Research University, 1 rue Jussieu, F-75005 Paris, France
[*]Corresponding author: clement.cabriel@u-psud.fr
[**]E-mail: sandrine.leveque-fort@u-psud.fr

August 6, 2018

We developed a 3D localization-based super-resolution technique providing an almost isotropic 3D resolution over a 1 µm range with precisions down to 15 nm. The axial localization is performed through a combination of point spread function (PSF) shaping and supercritical angle fluorescence (SAF), which yields absolute axial information. Using a dual-view scheme, the axial detection is decoupled from the lateral detection and optimized independently. This method can be readily implemented on most homemade PSF shaping setups and provides drift-free, tilt-insensitive and achromatic results. Its insensitivity to these unavoidable experimental biases is especially adapted for multicolor 3D super-resolution microscopy, as we demonstrate by imaging cell cytoskeleton, living bacteria membranes and axon periodic submembrane scaffolds. We further illustrate the interest of the technique for biological multicolor imaging over a several µm range by direct merging of multiple acquisitions at different depths.

Despite recent advances in localization-based super-resolution techniques, 3D fluorescence imaging of biological samples remains a major challenge, mostly because of its lack of versatility. While photoactivated localization microscopy (PALM) and (direct) stochastic optical reconstruction microscopy ((d)STORM) can easily provide lateral a localization precision (i.e. the standard deviation of the position) down to 5–10 nm [1, 2, 3, 4], a great deal of effort is being made to develop quantitative and reproducible 3D super-localization methods. The most widely used 3D SMLM technique is the astigmatic imaging, which relies on the use of a cylindrical lens to apply an astigmatic aberration in the detection path to encode the axial information in the shape of the spots, achieving an axial localization precision down to 20–25 nm [5]—though the precision varies with the axial position. Other Point Spread Function (PSF) shaping methods are also available [6, 7, 8], but their implementations are not as inexpensive and straightforward. Still, all PSF shaping methods including astigmatic imaging suffer from several drawbacks such as axial drifts, chromatic aberration, field-varying geometrical aberrations and sample tilts. These sources of biases often degrade the resolution or hinder

bioRxiv preprint doi: https://doi.org/10.1101/385799; this version posted August 6, 2018. The copyright holder for this preprint (which was not certified by peer review) is the author/funder. All rights reserved. No reuse allowed without permission.

colocalization and experiment reproducibility. Axial measurements can also be performed thanks to intensity-based techniques like Supercritical Angle Fluorescence (SAF) [9, 10, 11, 12, 13, 14], which relies on the detection of the near-field emission of fluorophores coupled into propagative waves at the sample/glass coverslip interface due to the index mismatch. Combined with SMLM, this technique, called Direct Optical Nanoscopy with Axially Localized Detection (DONALD), yields absolute axial positions (i.e. independent of the focus position) in the first 500 nm beyond the coverslip with a precision down to 15 nm [15, 16].

We set out to develop a microscopy technique that offers precise and unbiased results to enable reliable quantitative biological studies. Starting from the efficient and straightforward astigmatic imaging, we propose to push back its previously mentioned limits thanks to a novel approach based on a dual-view setup (**Fig. 1a**) that combines two features. First, it decouples the lateral and axial detections to optimize the 3D localization precision, and second, it uses two different sources of axial information: a strong astigmatism-based PSF measurement is merged with a complementary DONALD information that provides an absolute reference. This reference is crucial to render the axial detection insensitive to axial drifts and sample tilts as well as chromatic aberrations: unlike most other techniques that use fiducial markers [17] or structure correlations [5] to provide these corrections, here we intend to use the fluorophores themselves as absolute and biases-insensitive references. Besides, by applying a large astigmatic aberration on one fluorescence path only, this technique optimizes the axial precision for the collected photon number (**Supplementary Fig. 1**) and maintains a slowly varying localization precision over the imaging depth. Unlike most PSF shaping implementations found in the literature, which use moderate aberrations [5, 18, 19] to preserve the lateral resolution, the dual path detection allows one to fully benefit from the astigmatism capabilities. Indeed, as the lateral detection is mostly provided by the aberration-free path, the strong PSF shaping does not compromise the lateral detection. In order to merge the axial and lateral information sources, each is assigned a relative weight according to its localization precision (see **Fig. 1b** and **Methods**). Such a setup exhibits a major advantage in terms of axial precision despite only half of the photons being used for the axial localization far from the coverslip compared to a standard single-view PSF measurement microscope. As a result, this technique, called Dual-view Astigmatic Imaging with SAF Yield (DAISY), exhibits an almost isotropic resolution. We first performed the calibration of the astigmatism-based axial detection using 15 µm diameter latex microspheres coated with Alexa Fluor (AF) 647 as described in [20] in order to account for the influence of the optical aberrations on the PSFs and thus eliminate potential axial bias sources. Then, to evaluate the localization precision, we imaged dark red 40 nm diameter fluorescent beads (F8789, Thermo Fisher) located at various randomly distributed heights with a 637 nm excitation with DAISY (**Fig. 1c**). As it takes advantage of the good performance of the SAF detection near the coverslip, DAISY exhibits a resolution that slowly varies with the depth: the lateral and axial precisions reach values as low as 8 nm and 12 nm respectively, and they both remain inferior to 20 nm in the first 600 nm. In comparison, common astigmatism implementations provide at best 20–25 nm axial precision [5] and only in a limited axial range of approximately 200–300 nm as according to CRLB calculations (**Supplementary Fig. 1a**)—only the dual-objective implementation achieves better precisions, at the cost of a much increased complexity [21].

Our technique thus provides precise 3D super resolution images (**Fig. 1d–e**); still, at this precision level, any experimental uncertainty or bias can have a devastating effect on the quality of the obtained data. The first source of error that has to be dealt with is the drift that typically comes from a poor mechanical stability of the stage or from thermal drifts. Lateral drifts are well known and can often be easily corrected directly from the localized data using cross-correlation algorithms [22]. However, accounting for the axial drifts can be much more demanding since 3D cross-correlation algorithms require long calculation times unless they sacrifice precision. Tracking fiducial markers is also possible [17], but since it requires a specific sample preparation and uses a dedicated detection channel at a different wavelength, it is not very practical. It is worth noticing that most commercially available locking systems typically stabilize the focus position at ±30 nm at best (**Supplementary Fig. 2**), which is hardly sufficient for high resolution imaging. As positions are measured relative to the focus plane with PSF shape measurement methods, axial drifts induce large losses of resolution.

bioRxiv preprint doi: https://doi.org/10.1101/385799; this version posted August 6, 2018. The copyright holder for this preprint (which was not certified by peer review) is the author/funder. All rights reserved. No reuse allowed without permission.

On the contrary, SAF detection yields absolute results; thus it is not sensitive to drifts. We used this feature to provide a reliable drift correction algorithm: for each localization, the axial position detected with the SAF and the astigmatic modalities were correlated, which allowed us to monitor the focus drift and to consequently correct the astigmatism results. To highlight the importance of this correction, we plotted the x-z profile of a microtubule labelled with AF647 as a function of time with both an astigmatism-based detection and DAISY (**Fig. 2a**).

In the framework of quantitative biological studies, the axial detection can furthermore be hampered by the axial chromatic aberration due to the dispersion of the lenses, including the objective lens. If uncorrected, such a chromatic shift induces a bias in the results of multicolor sequential acquisitions, thus hindering colocalization. However, as DAISY provides absolute axial information thanks to the SAF measurement, it is not sensitive to this chromatic aberration. We performed a two-color sequential acquisition on microtubules labelled with AF647 and AF555 to illustrate the chromatic dependence inherent in standard PSF shaping detection (which exhibits chromatic shifts as large as 70 nm) and the insensitivity of DAISY to this effect (chromatic shift inferior to 5 nm) (**Fig. 2b**). Consequently, unbiased dual-color 3D images of biological samples can be obtained thanks to sequential acquisitions: we illustrate this on a sample with the actin and the tubulin labelled with AF647 and a 560-nm-excitable DNA-PAINT fluorophore (**Fig. 2c**).

It is well known that axial biases in PSF shaping measurements can further stem from tilts of the stage or sample holder, as well as from field-dependent geometrical optical aberrations. These issues were thoroughly studied by Diezmann *et al.*, who reported discrepancies higher than 100 nm over one field of view [23]. Although assessing tilts on biological samples is difficult with PSF measurement methods, DAISY makes this measurement straightforward since the absolute reference provided by the SAF detection can be used to measure the values of the astigmatic axial positions detected for molecules at the coverslip as a function of their lateral positions and then correct the tilt. We performed DAISY acquisitions on 20 nm diameter fluorescent beads at the coverslip and displayed the z values obtained with both an astigmatism-based detection and DAISY. While the former exhibits a clear tilt ranging from -30 nm to +30 nm over a 30 µm wide field, the latter is insensitive to the tilt, with less than 2 nm axial discrepancy between the two sides of the field (**Fig. 2d**). Aside from tilt effects, field-dependent aberrations also induce PSF shapes deformations, leading to axial biases. Although we do not actually perform corrections, DAISY is less sensitive to that effect compared to standard astigmatism imaging: on the one hand, the SAF detection relies on intensity measurement, and on the other hand, as DAISY uses a high astigmatism, i.e. strongly aberrated PSFs, it exhibits little sensitivity to remaining field aberrations. To illustrate this phenomenon, we compared tilt-corrected axial positions obtained with 20 nm diameter fluorescent beads deposited on a coverslip between a standard weaker astigmatic detection (350 nm between the two focal lines, close to the values commonly found in the literature) and DAISY. We got rid of the dispersion due to the localization precision by averaging the results over time for each bead and we plotted the corresponding detected depth histograms over one 30 µm wide field of view (**Supplementary Fig. 3**). The distribution widths evidence a much lower impact on the DAISY detection (standard deviation equal to 21 nm) than on the standard astigmatic detection (standard deviation equal to 45 nm).

Lastly, the optical aberrations applied in PSF shaping-based setups not only deform the PSFs, but they may also distort the field itself. For instance, when astigmatism is used, the system has two different focal lengths in x and y, which implies that the magnification is different in x and y. While this effect is of the order of a few per cent, it definitely biases the results whenever it is necessary to measure lateral distances precisely. With DAISY, evaluating this image distortion is straightforward thanks to the non-astigmatic detection path: a cross-correlation performed between the astigmatic and the unaberrated 2D SMLM images directly gives the magnification difference between the x and y axes, which accounts for 3.5% approximately in our case (**Fig. 2e**). By applying an affine transformation, the deformation is then corrected. It should be noticed, however, that a solution to avoid such a deformation would be to place the cylindrical lens in the Fourier plane, although most reported PSF shaping setups do not use this optical configuration. Also, more complex PSF shapes might induce complex field distortions—potentially making the correction more difficult.

To evidence the performances of DAISY for unbiased, reproducible and quantitative experiments,

bioRxiv preprint doi: https://doi.org/10.1101/385799; this version posted August 6, 2018. The copyright holder for this preprint (which was not certified by peer review) is the author/funder. All rights reserved. No reuse allowed without permission.

we used it to image biological samples. We illustrate the performances in terms of resolution by performing acquisitions on living *E. coli* bacteria adhered to a coverslip. The envelope of bacteria was labelled with both AF647 and AF555 using a click chemistry process (see **Methods**) [24, 25]. Since the lipopolysaccharide (LPS) layer is thin in Gram-negative bacteria, this is a good sample to observe the influence of the localization precision. We present in **Fig. 3a–b** 2D and 3D images of a region of interest and in **Fig. 3c** an x-z slice along the line displayed in **Fig. 3a**. The diameter of the bacterium is around 1 µm but still it does not exhibit a strong loss of resolution at its edges. To evidence this, we also plotted the lateral and axial histograms in the boxed regions (**Fig. 3c**). The axial standard deviations were found to be respectively around 30 nm and 45 nm at the bottom and at the top of the cell, while lateral standard deviations were around 27 nm in both colors. Taking into account the size of the LPS layer (<10 nm), of the label (10 nm) and the effect of the curvature of the bacterium over the width of the area used for the analysis (10 nm), these values are consistent with the localization precision curves plotted in **Fig. 1c**.

We then used DAISY to visualize the periodic submembrane scaffold present along the axon of cultured neurons [26]. We imaged the 3D organization of two proteins within this scaffold: adducin (labelled with AF647) that associates with the periodic actin rings, and β2-spectrin (labelled with AF555) that connect the actin rings (**Fig. 3d–f**). The lateral resolution allowed us to easily resolve the alternating patterns of adducin rings and β2-spectrin epitopes and their 190 nm periodicity (**Fig. 3g**) [27]. Thanks to the axial resolution of DAISY, we were also able to resolve the submembrane localization of both proteins across the whole diameter of the axon at 600 nm depth (**Fig. 3h**).

Taking advantage of the features of DAISY for unbiased sequential imaging, we propose an implementation allowing multicolor imaging at wider depths by stacking the results of multiple acquisitions on the same field at different heights. Although PSF measurement methods also allow this type of acquisitions, DAISY is especially suited in this case thanks to its previously described intrinsic bias correction features. Since the SAF signal quickly decays with the depth, the absolute reference is accessible only in the first stack associated with the first 500nm above the coverslip. As it provides unbiased results, the top of this first stack serves as an absolute reference for the next stack, which is matched to the previous using an axial position cross-correlation algorithm. We imaged a dual-label tubulin-clathrin sample (COS-7 cells, light chain- and heavy chain-clathrin labelled with AF647, α- and β-tubulin labelled with 560-nm-excitable DNA-PAINT imager) in three sequential acquisitions while shifting the focus by 500 nm between each of them to obtain a 3D dual-color 2 µm imaging range set of data (**Fig. 3i**). Aside from the fact that no axial mismatch between the subsequent acquisitions was observed, the localization precision remained satisfactory after 1.5 µm as it is limited only by the effect of the spherical aberration and sample-induced aberrations. To evidence this, we measured the dispersion of the localizations on two clathrin spheres located close to the ventral membrane (200 nm depth) and the dorsal membrane (1500 nm depth) respectively (**Fig. 3j**). The lateral and axial full widths at half maximum were found to be 38 nm in xy and 40 nm in z at 200 nm depth, and 47 nm in xy and 64 nm in z at 1500 nm depth—as expected, the axial precision is more affected by the effect of the aberrations in the volume than the lateral precision.

Thanks to the decoupling of the axial and lateral detections and to the combination of two axial SMLM techniques yielding complementary information, we could achieve reliable and unbiased imaging that enables quantitative studies on biological samples. DAISY offers an almost isotropic resolution over the whole micron-wide capture range, with a localization precision down to 15 nm. Thanks to both the SAF and the astigmatic detections, DAISY provides absolute axial results that prove to be insensitive to axial drifts and sample tilts as well as chromatic aberration. These features make it especially suited for biological samples imaging near the coverslip, which finds applications in the framework of cell adhesion or motility processes or bacteria imaging. However, stacking acquisitions performed at different heights also enables reproducible and reliable studies at more important depths, up to a few µm. Finally, as the implementation of the dual-view detection scheme we use is straightforward, it would also benefit any PSF measurement methods other than astigmatism, such as dual helix [6], self-bending PSF [7], saddle-point PSF [8] and tetrapod [28], which offer better performances in terms of localization precision and capture range.

bioRxiv preprint doi: https://doi.org/10.1101/385799; this version posted August 6, 2018. The copyright holder for this preprint (which was not certified by peer review) is the author/funder. All rights reserved. No reuse allowed without permission.

Acknowledgements

We thank Ultivue for consumable gifts and Abbelight for software and buffers gifts.
We acknowledge the contribution of the Centre de Photonique BioMédicale to cell culture and labelling. We also acknowledge the help of Marion Bardou with cell culture. Finally, we thank Caroline Schou and Yann Kergutuil for their help regarding software analysis.
This work was supported by the AXA research fund, the ANR (LABEX WIFI, ANR-10-LABX-24), the DIM CNANO Île-de-France, the IRS Bioprobe and the Mission interdisciplinarité of the CNRS.

Author contributions

C.C., N.B., P.J., G.D., E.F. and S.L.-F. conceived the project. C.C. designed the optical setup and performed the acquisitions. C.C. and N.B. carried out simulations and data analysis. C.C. and P.J. performed the CRLB calculations. N.B. developed the (d)STORM buffer. N.B., C.C. and P.J. optimized the immunofluorescence protocol. P.J. and C.C. prepared the COS-7 cells samples, C.L. prepared the neuron samples, A.B., M.-A. B.-D. and B.V. prepared the bacteria samples. All authors contributed to writing the manuscript.

Competing financial interests

N.B., E.F. and S.L.F. are shareholders in Abbelight.

bioRxiv preprint doi: https://doi.org/10.1101/385799; this version posted August 6, 2018. The copyright holder for this preprint (which was not certified by peer review) is the author/funder. All rights reserved. No reuse allowed without permission.

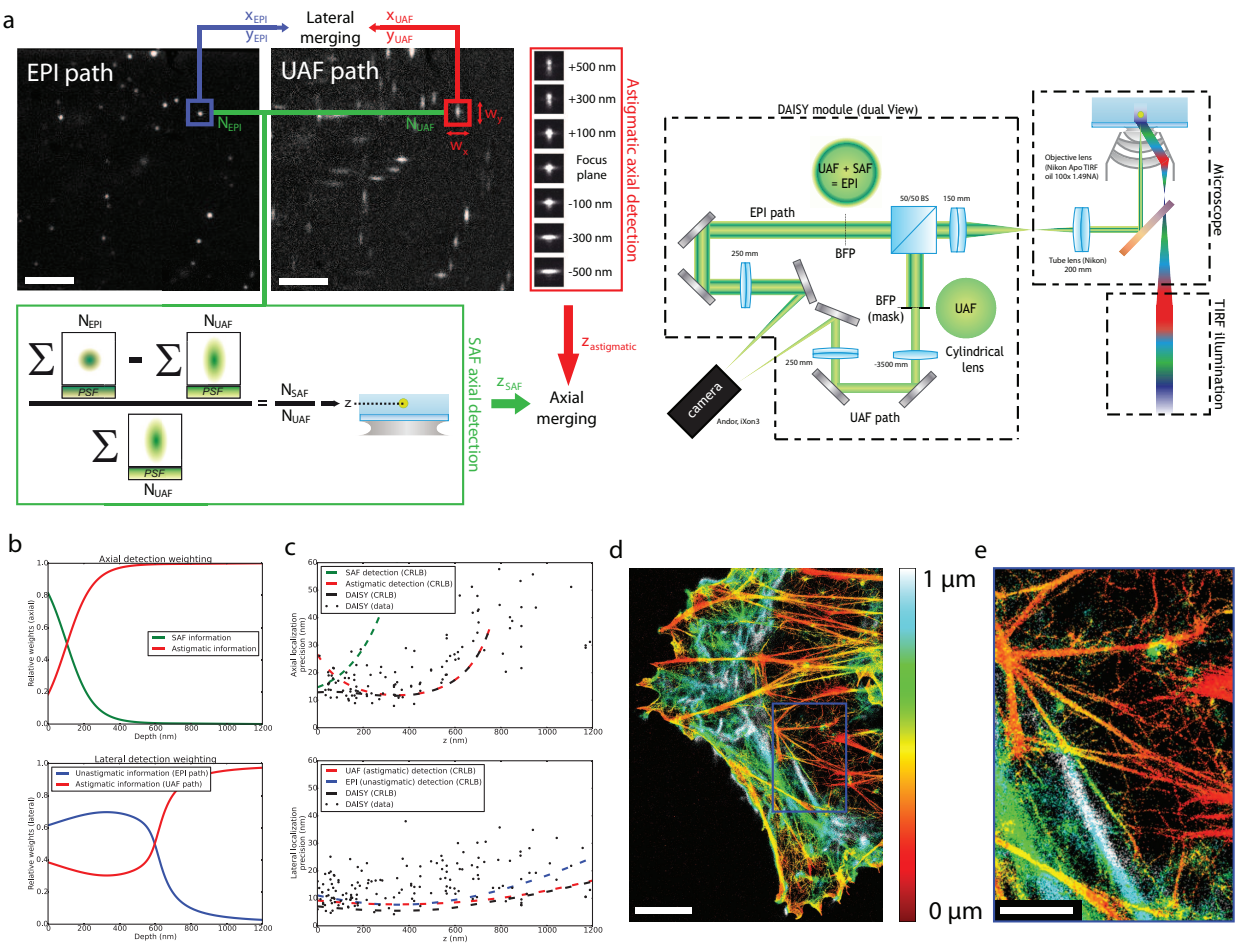

Figure 1: Description of the principle of DAISY and characterization of the precision. **(a)** Schematic of the setup. The DAISY module is placed between the microscope and the camera. After the beam splitter cube (BS), the UAF path contains a cylindrical lens, as well as a physical mask in a relay plane of the back focal plane of the objective to block the SAF photons. These two elements are not present in the EPI detection path. The images are formed on the two halves of the same camera. UAF and EPI frames recorded by the camera on a given field (COS-7 cells, α-tubulin immunolabelling, Alexa Fluor 647) are also displayed. For each PSF, the x and y widths are measured to obtain the astigmatic axial information, and the numbers of UAF and EPI photons are used to retrieve the SAF axial information. Finally, the lateral positions are obtained by merging the lateral positions from the UAF and EPI paths. **(b)** Relative weights of the SAF and astigmatic axial detections (top) and of the UAF and EPI lateral positions (bottom) used to merge the positions in DAISY (see **Methods** for the exact formulas). **(c)** Axial (top) and lateral (bottom) precisions of DAISY. The experimental data were taken on dark red 40 nm fluorescent beads distributed at various depths, each emitting a total number of photons around 5500 (similar to Alexa Fluor 647). 500 frames were acquired and the precisions were evaluated from the dispersion of the results for each bead. The Cramér-Rao Lower Bound (CRLB) contributions of each detection modality are also displayed, as well as the CRLB of DAISY for typical experimental conditions. **(d)** 3D (color-coded depth) DAISY image of actin (COS-7 cell, AF647-phalloidin labelling). **(e)** Zoom on the boxed region displayed in **(d)**. Scale bars: 5 µm **(a)** and **(d)**, 2 µm **(e)**.

bioRxiv preprint doi: https://doi.org/10.1101/385799; this version posted August 6, 2018. The copyright holder for this preprint (which was not certified by peer review) is the author/funder. All rights reserved. No reuse allowed without permission.

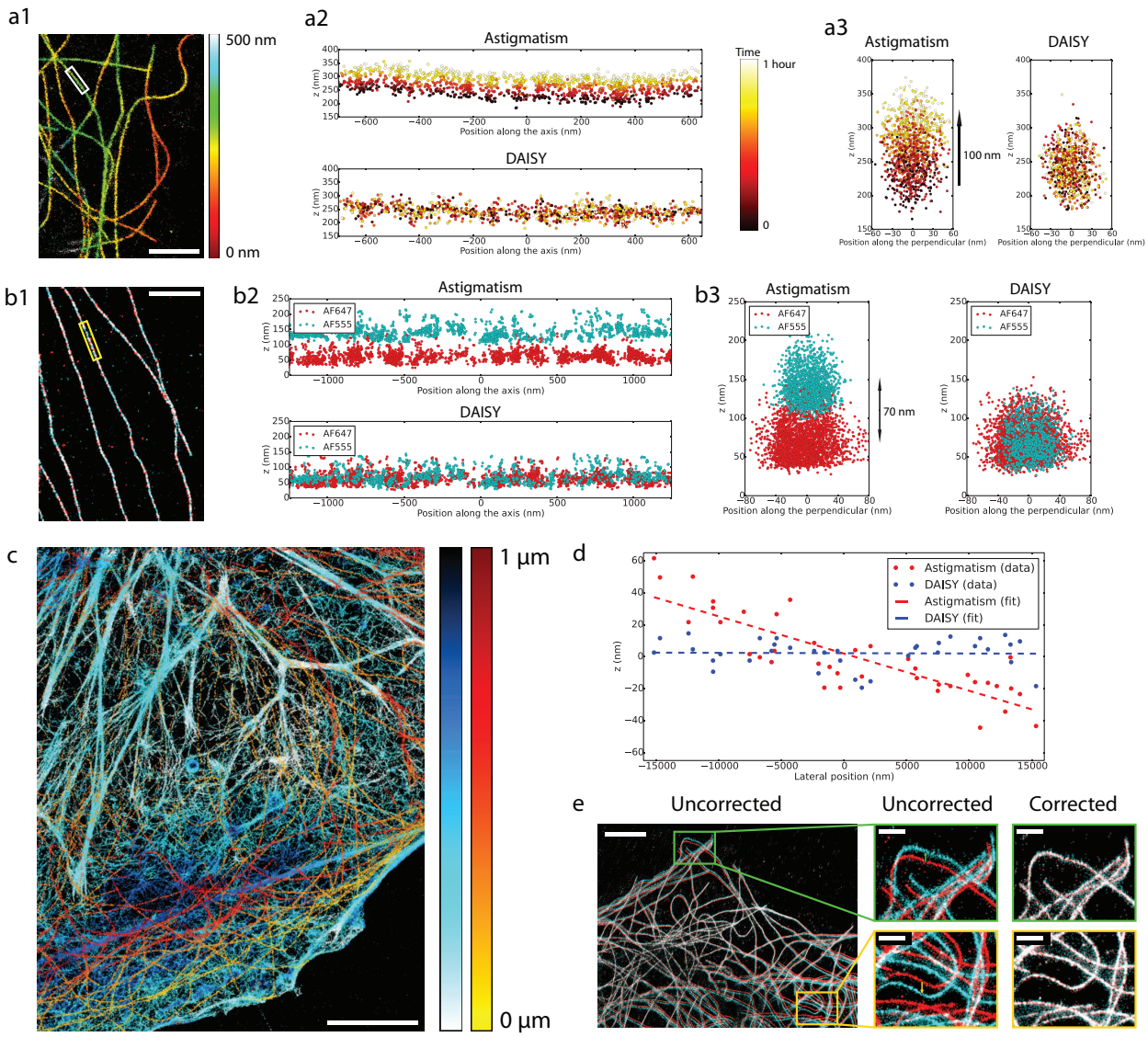

Figure 2: Characterization of the performances of DAISY. **(a)** Illustration of the effect of axial drifts. **(a1)** depth map of microtubules (COS-7 cells, α-tubulin labelled with AF647). The x-z **(a2)** and y-z **(a3)** profiles of the boxed microtubule are plotted for both standard astigmatic imaging and DAISY. The time is color-coded over one hour to highlight the effect of the temporal drift. **(b)** Effect of the chromatic aberration. **(b1)** 2D localization image of microtubules (COS-7 cells, α-tubulin labelled with AF555 and β-tubulin labelled with AF647) sequentially imaged in two different colors (red: AF647, cyan: AF555). The x-z **(b2)** and y-z **(b3)** profiles of the boxed microtubule are plotted for both standard astigmatic imaging and DAISY. The time is color-coded. **(c)** Dual-color depth map of actin (cyan-blue) and tubulin (yellow-red) in COS-7 cells (actin labelled with AF647-phalloidin and α-tubulin labelled with DNA-PAINT and imaged with an imager at 560 nm). **(d)** Influence of the sample tilt on the axial detection. The same field (20 nm dark red fluorescent beads deposited on a coverslip) was imaged with both standard astigmatic imaging and DAISY and the results were averaged over 500 frames to suppress the influence of the localization precision. The detected depth profile is plotted along the tilt axis. **(e)** Illustration of the image deformation induced by the astigmatism. For the same acquisition (COS-7 cells, α-tubulin labelled with AF647), 2D images were reconstructed from the lateral positions measured on both the astigmatic UAF (in cyan) and the unastigmatic EPI (in red) detection paths of our setup, before the deformation correction (left) and after (right). The whole field and zooms on the boxed regions are both displayed. Scale bars: 2 µm **(a1–b1)**, 5 µm **(c)** and **(e)** left, 1 µm **(e)** right insets.

bioRxiv preprint doi: https://doi.org/10.1101/385799; this version posted August 6, 2018. The copyright holder for this preprint (which was not certified by peer review) is the author/funder. All rights reserved. No reuse allowed without permission.

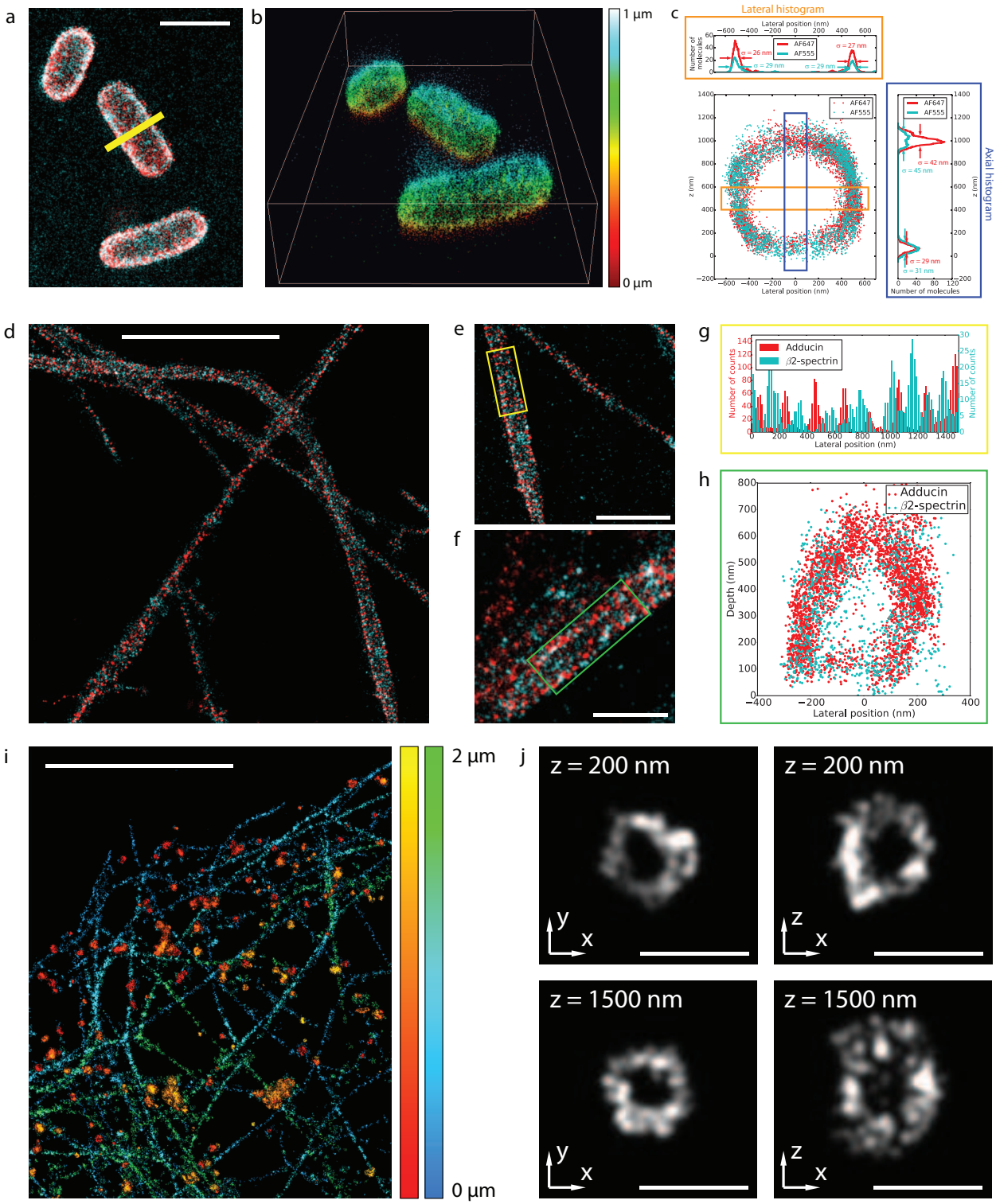

Figure 3: DAISY results obtained from biological samples. **(a)** 2D SMLM image of living *E. coli* bacteria labelled with both AF647 and AF555 at the membrane. **(b)** 3D view of the field displayed in **(a)**. The depth is color-coded (one single colormap is used for both AF647 and AF555). **(c)** x-z slice along the line displayed in **(a)** and axial and lateral profiles in the boxed regions. **(d)**, **(e)** and **(f)** 2D dual-color images of rat hippocampal neurons where the adducin and the β2-spectrin were labelled with AF647 and AF555 respectively. **(g)** Lateral profile along the axis of the yellow box displayed in **(e)**. **(h)** x-z slice along the green box displayed in **(f)**. **(i)** 3D extended range dual color image of clathrin (red-yellow) and tubulin (blue-green) obtained from three sequential acquisitions at different heights. **(j)** x-y and x-z slices of two clathrin spheres taken from **(i)** at two different depths (200 nm and 1500 nm). Scale bars: 2 µm **(a)**, 5 µm **(d)**, 2 µm **(e)**, 1 µm **(f)**, 5 µm **(i)**, 500 nm **(j)**.

bioRxiv preprint doi: https://doi.org/10.1101/385799; this version posted August 6, 2018. The copyright holder for this preprint (which was not certified by peer review) is the author/funder. All rights reserved. No reuse allowed without permission.

Methods

Optical setup. A schematic of the optical setup used is presented in **Fig. 1a**. We used a Nikon Eclipse Ti inverted microscope with a Nikon Perfect Focus System. The excitation was performed thanks to five different lasers: 637 nm (Obis 637LX, 140 mW, Coherent), 561 nm (Genesis MX 561 STM, 500 mW), 532 nm (Verdi G5, 5 W, Coherent), 488 nm (Genesis MX 488 STM, 500 mW, Coherent) and 405 nm (Obis 405LX, 100 mW, Coherent). The corresponding 390/482/532/640 or 390/482/561/640 multiband filters (LF405/488/532/635-A-000 and LF405/488/561/635-A-000, Semrock) were used. The fluorescence was collected through a Nikon APO TIRF x100 1.49 NA oil immersion objective lens, sent in the DAISY module and recorded on two halves of a 512x512-pixel EMCCD camera (iXon3, Andor). The camera was placed at the focal plane of the module of magnification 1.67 and the optical pixel size was approximately 100 nm. Finally, the imaging paths were calibrated in intensity to compensate the non-ideality of the 50-50 beam splitter as well as the reflection on the cylindrical lens surface (this measurement was performed for each fluorescence wavelength). The object focal plane of the EPI path was typically at the coverslip ($z = 0$ nm) and the UAF path had two focal lines, at $z = 0$ nm and $z = 800$ nm for the y and x axes respectively.

Sample preparation. COS-7 cells were grown in DMEM with 10% FBS, 1% L-glutamin and 1% penicillin/streptomycin (Life Technologies) at 37°C and 5% CO_2 in a cell culture incubator. Several days later, they could be plated at low confluency on cleaned round 25 mm diameter high resolution #1.5 glass coverslips (Marienfield, VWR). After 24 hours, the cells were washed three times with PHEM solution (60 mM PIPES, 25 mM HEPES, 5 mM EGTA and 2 mM Mg acetate adjusted to pH 6.9 with 1 M KOH) and fixed for 20 min in 4% PFA, 0.02% glutaraldehyde and 0.5% Triton; they were then washed 3 times in PBS (Invitrogen, 003000). Up to this fixation step, all chemical reagents were pre-warmed at 37°C. The cells were post-fixed for 10 min with PBS + 0.1% Triton X-100, reduced for 10 min with $NaBH_4$, and washed in PBS three times before being blocked for 15 min in PBS + 1% BSA.
The labelling step varied according to the required sample: in the case of actin labelling, the cells were incubated for 20 minutes with 3.3 nM phalloidin-AF647 (Thermo Fisher, A22287) in the (d)STORM imaging buffer (Abbelight) before starting the acquisition—without removing the (d)STORM buffer containing the phalloidin-AF647. On the contrary, immunolabelling of tubulin and clathrin required more preparation steps.
For AF647 α-tubulin, the cells were incubated for 1 hour at 37°C with 1:300 mouse anti-α-tubulin antibody (Sigma Aldrich, T6199) in PBS + 1% BSA. This was followed by three washing steps in PBS + 1% BSA, incubation for 45 min at 37°C with 1:300 goat anti-mouse AF647 antibody (Life Technologies, A21237) diluted in PBS 1% BSA and three more washes in PBS.
For AF647 β-tubulin and AF555 α-tubulin, the cells were incubated for 1 hour at 37°C with 1:300 rabbit anti-β-tubulin antibody (Abcam, ab6046) in PBS + 1% BSA. This was followed by three washing steps in PBS + 1% BSA, incubation for 45 min at 37°C with 1:300 goat anti-rabbit AF555 antibody (Life Technologies, A21430) diluted in PBS + 1% BSA and three more washes in PBS + 1% BSA. Then they were incubated again for 1 hour at 37°C with 1:300 mouse anti-α-tubulin antibody (Sigma Aldrich, T6199) in PBS + 1% BSA, washed three times, incubated for 45 min at 37°C with 1:300 goat anti-mouse AF647 antibody (Life Technologies, A21237) diluted in PBS + 1% BSA and washed three more washes in PBS.
For AF647 heavy chain and light chain clathrin and DNA-PAINT α- and β-tubulin, the cells were incubated for 1 hour at 37°C with 1:400 mouse anti-light chain clathrin antibody (Sigma Aldrich, C1985) in PBS + 1% BSA and washed three times with PBS + 1% BSA, incubated again for 1 hour at 37°C with 1:400 mouse anti-heavy chain clathrin antibody (Sigma Aldrich, C1860) in PBS + 1% BSA and washed three times with PBS + 1% BSA. Then they were incubated for 45 min at 37°C with 1:400 anti-mouse AF647 antibody (Life Technologies, A21237) in PBS + 1% BSA, washed three times with PBS + 1% BSA, and incubated again for 1 hour at room temperature with 1:400 mouse β-tubulin antibody (Sigma Aldrich, T5293) in PBS + 1% BSA. This was followed by three washing steps in PBS + 1% BSA, incubation for 1 hour at 37°C with 1:400 mouse α-tubulin antibody (Sigma Aldrich, T6199) diluted in PBS 1% BSA, three more washes in PBS + 1% BSA, incubation for 2 hours at 37°C with 1:100 anti-mouse-D1 Ultivue secondary antibody antibody diluted in antibody dilution buffer

bioRxiv preprint doi: https://doi.org/10.1101/385799; this version posted August 6, 2018. The copyright holder for this preprint (which was not certified by peer review) is the author/funder. All rights reserved. No reuse allowed without permission.

(Ultivue) and washed three more washes in PBS.
In any case, after the immunolabelling of tubulin and/or clathrin, a post-fixation step was performed using PBS with 3.6% formaldehyde for 15 min. The cells were washed in PBS three times and then reduced for 10 min with 50 mM NH_4Cl (Sigma Aldrich, 254134), followed by three additional washes in PBS.
To prepare the neuron samples, rat hippocampal neurons from E18 pups were cultured on 18 mm coverslips at a density of 6,000/cm^2 according to previously published protocols [29] and following guidelines established by the European Animal Care and Use Committee (86/609/CEE) and approval of the local ethics committee (agreement D18-055-8). After 16 days in culture, neurons were fixed using 4% PFA in PEM (80 mM Pipes, 5 mM EGTA, and 2 mM $MgCl_2$, pH 6.8) for 10 min. After rinses in 0.1 M phosphate buffer (PB), neurons were blocked for 60 minutes at r. t. in immunocytochemistry buffer (ICC: 0.22% gelatin, 0.1% Triton X-100 in PB). Following this, neurons were incubated with a chicken primary antibody against map2 (abcam, ab5392) mouse primary antibody against β2-spectrin (BD Bioscience, 612563) and a rabbit primary antibody against adducin (abcam, ab51130) diluted in ICC overnight at 4°C, then after ICC rinses with AF 488, 555 and 647 conjugated secondary antibodies for 1h at 23°C.
The *E. coli* K12 (MG1655) cells were grown in 2YT medium (Sigma, Tryptone 16.0 g/L, Yeast extract 10.0 g/L, NaCl 5.0 g/L) at 37°C under agitation (180 rpm). Overnight cultures were diluted 100 times in fresh medium (final volume 300 µL) containing Kdo-N_3 (1.0 mM). Bacteria were incubated at 37°C for 9 hours under agitation (180 rpm). Then 200 µL of the obtained suspension were washed 3 times with PBS buffer (200 µL, 12 000 rpm, 1 min, r. t.). The pellet was re-suspended in 200 µL of a solution of DBCO-Sulfo-Biotin (JenaBioscience, CLK-A116) (0.50 mM in PBS buffer) and the suspension was vigorously agitated for 90 min at room temperature. Bacteria were washed 3 times with PBS buffer (200 µL, 12 000 rpm, 1 min, r. t.). The pellet was re-suspended in a solution of Streptavidin-AF647 / Streptavidin-AF555 (20 µg/mL each) (Invitrogen, ThermoFischer Scientific, S21374 and S32355) in PBS containing BSA (1.0 mg/mL, 200 µL) and the suspension was agitated at room temperature for 90 min in the dark. Bacteria were then washed 3 times with PBS buffer (200 µL, 12 000 rpm, 1 min, r. t.). The pellet was re-suspended in PBS buffer (400 µL) and stored at 4°C until analysis.

Image acquisition. (d)STORM/DNA-PAINT imaging on biological samples was performed using an oblique epifluorescence illumination configuration. To induce most of the molecules in a dark state, we used either a (d)STORM buffer (Abbelight Smart kit) or a dilution of DNA-PAINT imagers in imaging buffer. In both cases, the sample was lit with an irradiance of approximately 4 kW.cm^{-2} until a sufficient density of molecules was obtained (typically one molecule per 4 µm^2). We then started the data acquisition with 50 ms (for AF647) or 100 ms (for AF555 and DNA-PAINT imagers) exposure time and 150 EMCCD gain. The total number of acquired frames was typically between 15.000 and 30.000 per acquisition.
Performance measurements on fluorescent beads were done at low illumination powers (0.15 kW.cm^{-2} for 20 nm diameter dark red beads and 0.025 kW.cm^{-2} for tetraspeck beads and 40 nm diameter dark red beads). The beads were immersed in PBS and the exposure times and EMCCD gain were 50 ms and 150 respectively. Except for the long-term axial drift tracking experiment, 500 frames were recorded for each performance characterization acquisition.
The acquisition was performed using the Nemo software (Abbelight).

Localization software. Each 512x512-pixel frame was pre-processed by removing the pixel per pixel temporal median of the previous 10 frames in order to get rid of the slowly varying background without altering the number of photons in the PSFs. The filtered frames were then split in two parts corresponding to the UAF and EPI paths of the DAISY module respectively. On the 512x256-pixel sub-frames, the PSFs were detected using a wavelet filtering associated with an intensity threshold. Each PSF was characterized using a center of mass detection to retrieve the lateral positions x^{EPI}, y^{EPI}, x^{UAF} and y^{UAF}, and a Gaussian fitting to assess the PSF widths w_x^{UAF} and w_y^{UAF}. A photon counting was also performed over a 2 µm x 2 µm square area centered on the PSF to determine the number of photons N^{EPI} and N^{UAF}. A filtering step based on photon numbers and PSF widths was then operated to get rid of false positive detections. Corrections were applied to photon numbers

bioRxiv preprint doi: https://doi.org/10.1101/385799; this version posted August 6, 2018. The copyright holder for this preprint (which was not certified by peer review) is the author/funder. All rights reserved. No reuse allowed without permission.

(as mentioned in the **Optical setup** section) and lateral positions x^{UAF} and y^{UAF} (to compensate the image deformation induced by the astigmatism as illustrated in **Fig. 2e**). Afterwards, the axial positions were calculated: the values of z^{SAF} were obtained using the theoretical curve provided in [15] whereas those of $z^{astigmatic}$ could be retrieved by fitting $w_x^{UAF} - w_y^{UAF}$ to the calibration curve using a least squares calculation. Lateral drifts were then corrected using a temporal cross-correlation algorithm.
Finally, the values of z^{SAF} and $z^{astigmatic}$ were merged together, as well as the values of x^{EPI} and x^{UAF}, y^{EPI} and y^{UAF} (as described in the **Position merging** section).
All this processing was performed using a home-written Python code.

Position merging. In DAISY acquisitions, the lateral positions were obtained by combining the two sources of lateral information according to their uncertainties (the CRLB values were used for that purpose). The exact formula follows the normal distribution combination law:

$$x^{DAISY} = \left(\frac{x^{UAF}}{(\sigma_x^{UAF})^2} + \frac{x^{EPI}}{(\sigma_x^{EPI})^2} \right) \Big/ \left(\frac{1}{(\sigma_x^{UAF})^2} + \frac{1}{(\sigma_x^{EPI})^2} \right) \tag{1}$$

$$y^{DAISY} = \left(\frac{y^{UAF}}{(\sigma_y^{UAF})^2} + \frac{y^{EPI}}{(\sigma_y^{EPI})^2} \right) \Big/ \left(\frac{1}{(\sigma_y^{UAF})^2} + \frac{1}{(\sigma_y^{EPI})^2} \right) \tag{2}$$

where σ_i^{UAF} and σ_i^{EPI} are the localization precisions in the direction i for the UAF and EPI detections respectively (i.e. the standard deviations of the positions).
Similarly, the two sources of axial information were merged according to their uncertainties:

$$z^{DAISY} = \left(\frac{z^{SAF}}{(\sigma_z^{SAF})^2} + \frac{z^{astigmatic}}{(\sigma_z^{astigmatic})^2} \right) \Big/ \left(\frac{1}{(\sigma_z^{SAF})^2} + \frac{1}{(\sigma_z^{astigmatic})^2} \right) \tag{3}$$

where σ_z^{SAF} and $\sigma_z^{astigmatic}$ are the axial localization precisions of the SAF and the astigmatic detections respectively.
The relative weights used for DAISY are shown in **Fig. 1b**. It is worth noting that since localization precisions vary with the depth, the corresponding weights vary accordingly. Notably, the weight of the SAF detection is more important than that of the axial astigmatic detection at the coverslip, but it quickly dwindles to almost zero after 500 nm. Similarly, the (unastigmatic) EPI detection is more precise in the first depth of field, whereas the (astigmatic) UAF detection dominates after 600 nm, where the EPI PSFs are too defocused to be detected.

Localization precision measurement. The DAISY localization precision measurements displayed in **Fig. 1c** were performed on 40 nm diameter dark red fluorescent beads located at various heights. This was obtained by taking fixed, unlabelled COS-7 cells and adding 500 µL of beads solution diluted at 5.10^{-7} in PBS during 5 minutes for beads to deposit before removing the solution and replacing it with PBS. Beads stuck on the upper side of the membrane were thus located at random heights. The results of several 500-frame-acquisitions were pooled and for each of them, the lateral drift was corrected. The average axial position was measured for each bead, as well as the standard deviations on the lateral and axial measured positions, which gave the localization precisions.

3D visualization. The 3D view in **Fig. 3b** was obtained using the Nemo software (Abbelight).

Data availability. Data are available from the corresponding authors upon reasonable request.

References

[1] E. Betzig, G. H. Patterson, R. Sougrat, O. W. Lindwasser, S. Olenych, J. S. Bonifacino, M. W. Davidson, J. Lippincott-Schwartz, and H. F. Hess, "Imaging intracellular fluorescent proteins at nanometer resolution.," *Science (New York, N.Y.)*, vol. 313, pp. 1642–5, sep 2006.

bioRxiv preprint doi: https://doi.org/10.1101/385799; this version posted August 6, 2018. The copyright holder for this preprint (which was not certified by peer review) is the author/funder. All rights reserved. No reuse allowed without permission.

[2] S. T. Hess, T. P. K. Girirajan, and M. D. Mason, "Ultra-high resolution imaging by fluorescence photoactivation localization microscopy.," *Biophysical journal*, vol. 91, pp. 4258–72, dec 2006.

[3] M. J. Rust, M. Bates, and X. Zhuang, "Sub-diffraction-limit imaging by stochastic optical reconstruction microscopy (STORM)," *Nature Methods*, vol. 3, pp. 793–796, aug 2006.

[4] S. van de Linde, A. Löschberger, T. Klein, M. Heidbreder, S. Wolter, M. Heilemann, and M. Sauer, "Direct stochastic optical reconstruction microscopy with standard fluorescent probes.," *Nature protocols*, vol. 6, pp. 991–1009, jul 2011.

[5] B. Huang, W. Wang, M. Bates, and X. Zhuang, "Three-Dimensional Super-Resolution Imaging by Stochastic Optical Reconstruction Microscopy," *Science*, vol. 319, no. 5864, pp. 810–813, 2008.

[6] S. R. P. Pavani, M. A. Thompson, J. S. Biteen, S. J. Lord, N. Liu, R. J. Twieg, R. Piestun, and W. E. Moerner, "Three-dimensional, single-molecule fluorescence imaging beyond the diffraction limit by using a double-helix point spread function.," *Proceedings of the National Academy of Sciences of the United States of America*, vol. 106, no. 9, pp. 2995–2999, 2009.

[7] S. Jia, J. C. Vaughan, and X. Zhuang, "Isotropic three-dimensional super-resolution imaging with a self-bending point spread function," *Nature Photonics*, vol. 8, pp. 302–306, mar 2014.

[8] Y. Shechtman, S. J. Sahl, A. S. Backer, and W. Moerner, "Optimal point spread function design for 3d imaging," *Physical Review Letters*, vol. 113, sep 2014.

[9] T. Ruckstuhl, J. Enderlein, S. Jung, and S. Seeger, "Forbidden light detection from single molecules," *Analytical chemistry*, vol. 72, pp. 2117–23, may 2000.

[10] C. M. Winterflood, T. Ruckstuhl, D. Verdes, and S. Seeger, "Nanometer Axial Resolution by Three-Dimensional Supercritical Angle Fluorescence Microscopy," *Physical Review Letters*, vol. 105, p. 108103, aug 2010.

[11] J. Enderlein, I. Gregor, and T. Ruckstuhl, "Imaging properties of supercritical angle fluorescence optics.," *Optics express*, vol. 19, pp. 8011–8, apr 2011.

[12] T. Barroca, K. Balaa, J. Delahaye, S. Lévêque-Fort, and E. Fort, "Full-field supercritical angle fluorescence microscopy for live cell imaging.," *Optics letters*, vol. 36, pp. 3051–3, aug 2011.

[13] T. Barroca, K. Balaa, S. Lévêque-Fort, and E. Fort, "Full-Field Near-Field Optical Microscope for Cell Imaging," *Physical Review Letters*, vol. 108, p. 218101, may 2012.

[14] D. Axelrod, "Evanescent excitation and emission in fluorescence microscopy.," *Biophysical journal*, vol. 104, pp. 1401–9, apr 2013.

[15] N. Bourg, C. Mayet, G. Dupuis, T. Barroca, P. Bon, S. Lécart, E. Fort, and S. Lévêque-Fort, "Direct optical nanoscopy with axially localized detection," *Nature Photonics*, vol. 9, pp. 587–593, aug 2015.

[16] J. Deschamps, M. Mund, and J. Ries, "3D superresolution microscopy by supercritical angle detection," *Optics Express*, vol. 22, p. 29081, nov 2014.

[17] A.-K. Gustavsson, P. N. Petrov, M. Y. Lee, Y. Shechtman, and W. E. Moerner, "3d single-molecule super-resolution microscopy with a tilted light sheet," *Nature Communications*, vol. 9, jan 2018.

[18] R. McGorty, J. Schnitzbauer, W. Zhang, and B. Huang, "Correction of depth-dependent aberrations in 3d single-molecule localization and super-resolution microscopy," *Optics Letters*, vol. 39, p. 275, jan 2014.

[19] Y. Li, M. Mund, P. Hoess, J. Deschamps, U. Matti, B. Nijmeijer, V. J. Sabinina, J. Ellenberg, I. Schoen, and J. Ries, "Real-time 3d single-molecule localization using experimental point spread functions," *Nature Methods*, vol. 15, pp. 367–369, apr 2018.

bioRxiv preprint doi: https://doi.org/10.1101/385799; this version posted August 6, 2018. The copyright holder for this preprint (which was not certified by peer review) is the author/funder. All rights reserved. No reuse allowed without permission.

[20] C. Cabriel, N. Bourg, G. Dupuis, and S. Lévêque-Fort, "Aberration-accounting calibration for 3d single-molecule localization microscopy," *Optics Letters*, vol. 43, p. 174, jan 2018.

[21] X. Xu, Ke;Babcock, Hazen P; Zhuang, "Dual-objective STORM reveals three-dimensional filament organization in the actin cytoskeleton," *Nature methods*, vol. 9, no. 2, pp. 185–188, 2012.

[22] Y. Wang, J. Schnitzbauer, Z. Hu, X. Li, Y. Cheng, Z.-L. Huang, and B. Huang, "Localization events-based sample drift correction for localization microscopy with redundant cross-correlation algorithm," *Optics Express*, vol. 22, p. 15982, jun 2014.

[23] A. von Diezmann, M. Y. Lee, M. D. Lew, and W. E. Moerner, "Correcting field-dependent aberrations with nanoscale accuracy in three-dimensional single-molecule localization microscopy," *Optica*, vol. 2, p. 985, nov 2015.

[24] A. Dumont, A. Malleron, M. Awwad, S. Dukan, and B. Vauzeilles, "Click-mediated labeling of bacterial membranes through metabolic modification of the lipopolysaccharide inner core," *Angewandte Chemie International Edition*, vol. 51, pp. 3143–3146, feb 2012.

[25] E. Fugier, A. Dumont, A. Malleron, E. Poquet, J. M. Pons, A. Baron, B. Vauzeilles, and S. Dukan, "Rapid and specific enrichment of culturable gram negative bacteria using non-lethal copper-free click chemistry coupled with magnetic beads separation," *PLOS ONE*, vol. 10, p. e0127700, jun 2015.

[26] M.-J. Papandréou and C. Leterrier, "The functional architecture of axonal actin," *Molecular and Cellular Neuroscience*, may 2018.

[27] K. Xu, G. Zhong, and X. Zhuang, "Actin, spectrin, and associated proteins form a periodic cytoskeletal structure in axons.," *Science (New York, N.Y.)*, vol. 339, pp. 452–6, jan 2013.

[28] Y. Shechtman, L. E. Weiss, A. S. Backer, S. J. Sahl, and W. E. Moerner, "Precise three-dimensional scan-free multiple-particle tracking over large axial ranges with tetrapod point spread functions," *Nano Letters*, vol. 15, pp. 4194–4199, jun 2015.

[29] S. Kaech and G. Banker, "Culturing hippocampal neurons," *Nature Protocols*, vol. 1, pp. 2406–2415, dec 2006.

bioRxiv preprint doi: https://doi.org/10.1101/385799; this version posted August 6, 2018. The copyright holder for this preprint (which was not certified by peer review) is the author/funder. All rights reserved. No reuse allowed without permission.

Supplementary material

Supplementary Figure 1: Influence of the depth and the astigmatism amplitude on the axial and lateral localization precisions on the Cramér-Rao Lower Bound (CRLB) theoretical limit.

Supplementary Figure 2: Long-term tracking of the axial drift.

Supplementary Figure 3: Influence of the remaining field aberrations on the axial detection after tilt correction.

bioRxiv preprint doi: https://doi.org/10.1101/385799; this version posted August 6, 2018. The copyright holder for this preprint (which was not certified by peer review) is the author/funder. All rights reserved. No reuse allowed without permission.

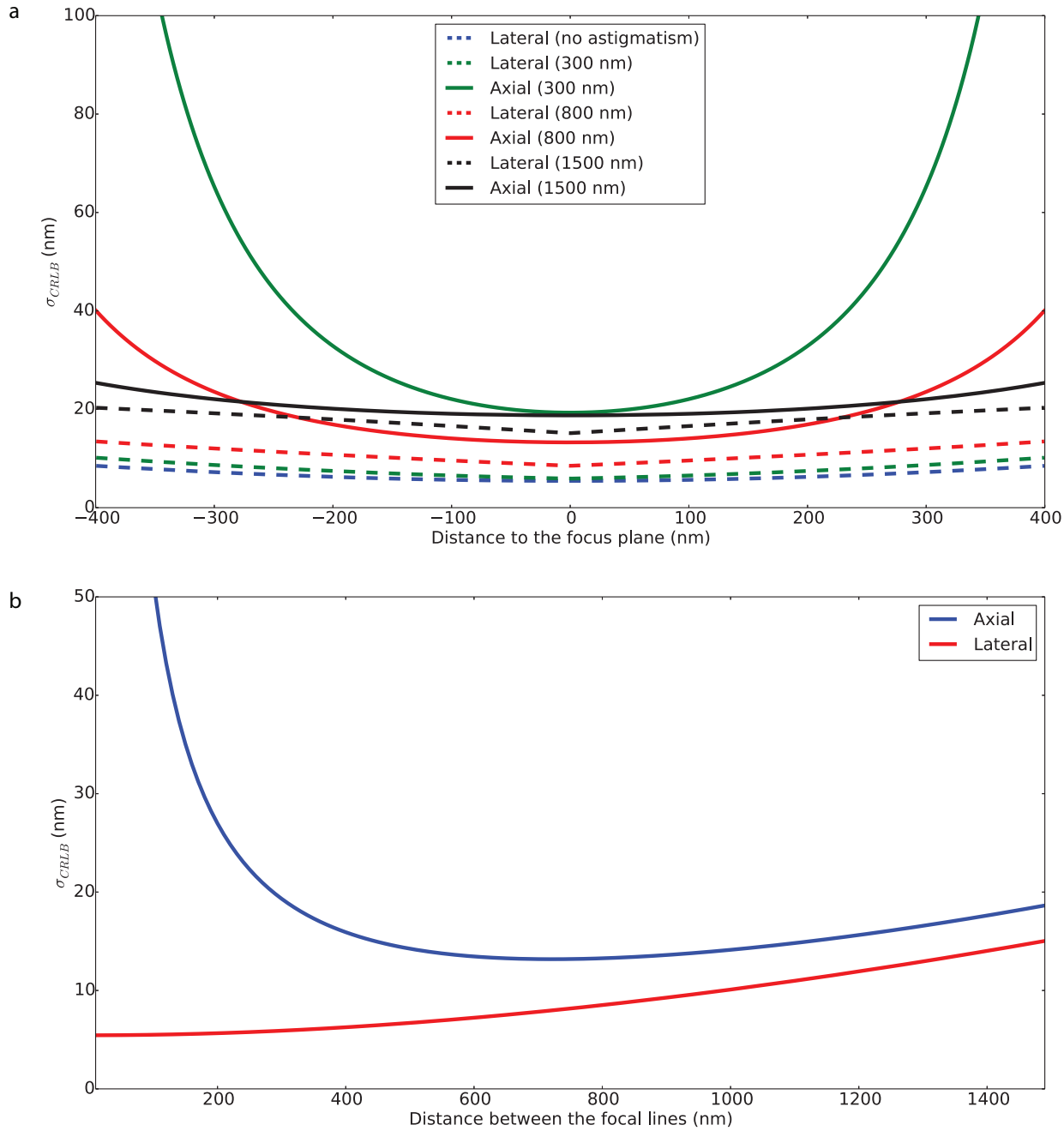

Supplementary Figure 1: Influence of the depth and the astigmatism amplitude on the axial and lateral localization precisions on the Cramér-Rao Lower Bound (CRLB) theoretical limit. **(a)** Variation of the localization precision with the distance to the focal plane for different astigmatism amplitudes (measured as the distance between the two focal lines in the object space, 300 nm being a typical value found in the literature and 800 nm being the value used for DAISY). The solid and dashed lines stand for the axial and lateral precisions respectively. The axial precision was calculated from the results published in [1]. **(b)** Influence of the astigmatism amplitude on the best achievable axial and lateral precisions (i.e. CRLB values at $z = 0$).

bioRxiv preprint doi: https://doi.org/10.1101/385799; this version posted August 6, 2018. The copyright holder for this preprint (which was not certified by peer review) is the author/funder. All rights reserved. No reuse allowed without permission.

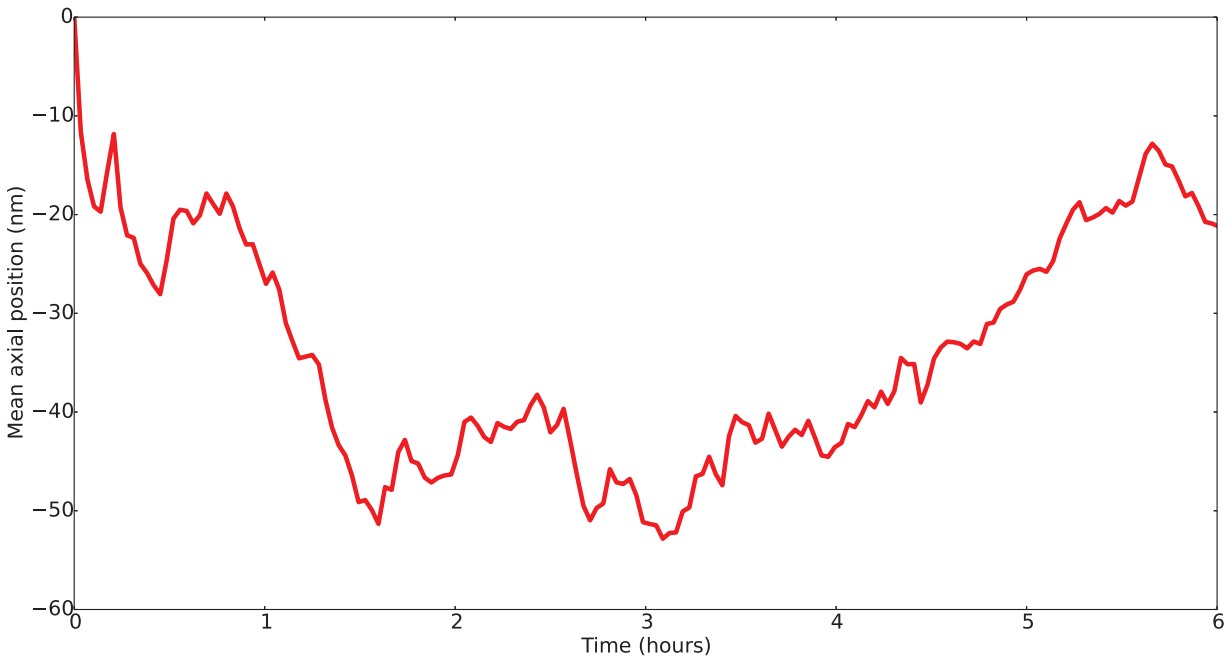

Supplementary Figure 2: Long-term tracking of the axial drift. The mean axial position of 100 nm diameter tetraspeck fluorescent beads (Thermo Fisher, T7279) over the imaged field is plotted as a function of time over approximately six hours. The results were averaged over 50 frames (i.e. 2.5 seconds) to suppress the influence of the localization uncertainty.

bioRxiv preprint doi: https://doi.org/10.1101/385799; this version posted August 6, 2018. The copyright holder for this preprint (which was not certified by peer review) is the author/funder. All rights reserved. No reuse allowed without permission.

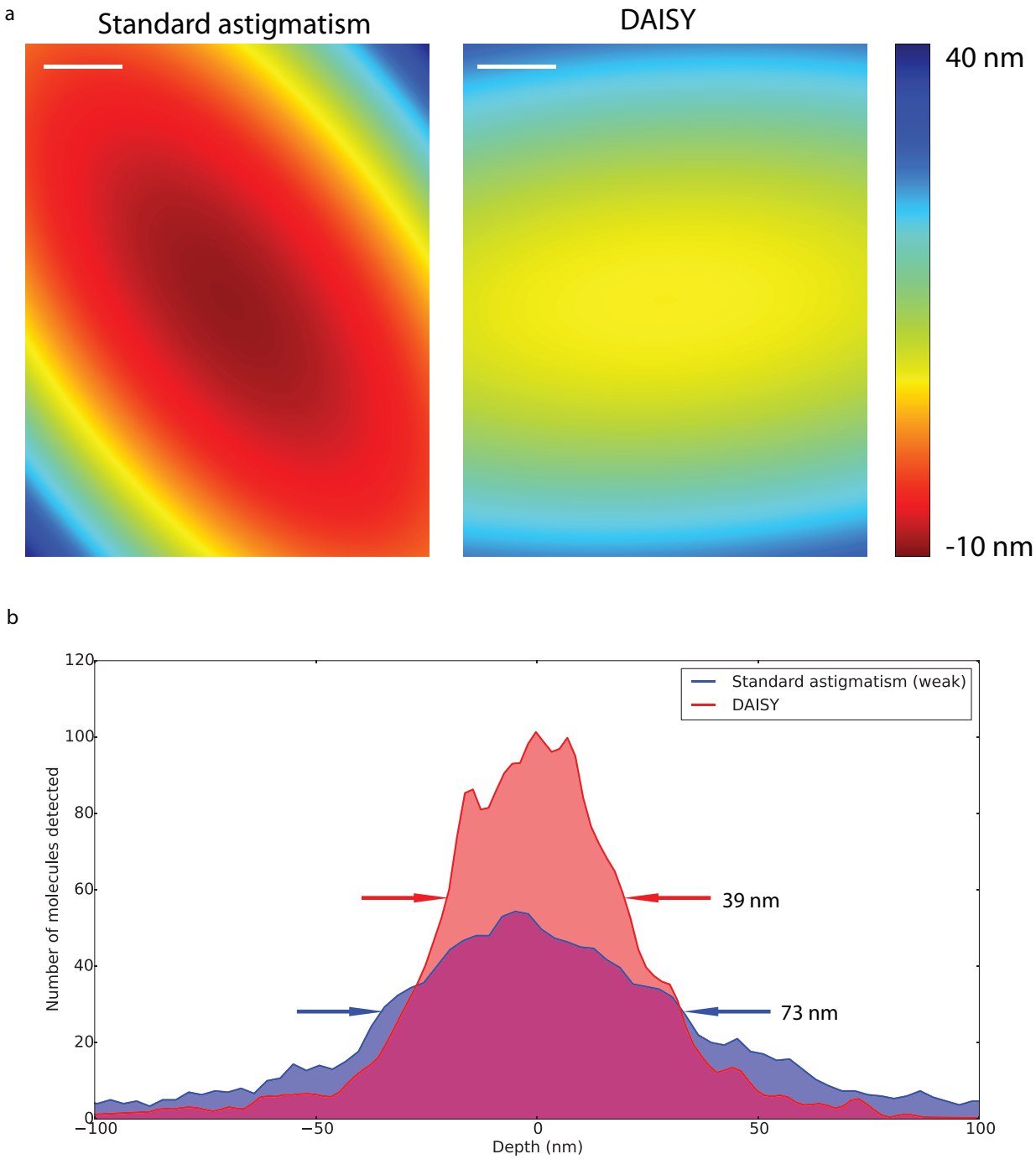

Supplementary Figure 3: Influence of the remaining field aberrations on the axial detection after tilt correction. **(a)** Interpolated depth maps of the axial positions measured for a sample of 20 nm dark red fluorescent beads deposited on a coverslip and averaged over 500 frames. The results are plotted for both a typical astigmatism-based imaging (300 nm spacing between the two focal lines, close to the values encountered in the literature) and for DAISY. **(b)** The depth histograms are plotted over the 30 µm wide field for both a typical astigmatic detection (300 nm between the two focal lines) and for DAISY. Scale bars: 5 µm.

bioRxiv preprint doi: https://doi.org/10.1101/385799; this version posted August 6, 2018. The copyright holder for this preprint (which was not certified by peer review) is the author/funder. All rights reserved. No reuse allowed without permission.

Supplementary reference

[1] B. Rieger and S. Stallinga, "The lateral and axial localization uncertainty in super-resolution light microscopy," *ChemPhysChem*, vol. 15, no. 4, pp. 664–670, 2014.